scientific reports

Check for updates

OPEN

Improved oxidation behavior of $Hf_{0.11}Al_{0.20}B_{0.69}$ in comparison to $Hf_{0.28}B_{0.72}$ magnetron sputtered thin films

Pauline Kümmerl[1]✉, Sebastian Lellig[1,2], Amir Hossein Navidi Kashani[1], Marcus Hans[1], Peter J. Pöllmann[1], Lukas Löfler[1], Ganesh Kumar Nayak[1], Damian M. Holzapfel[1], Szilárd Kolozsvári[3], Peter Polcik[3], Peter Schweizer[2], Daniel Primetzhofer[4], Johann Michler[2] & Jochen M. Schneider[1]

The oxidation resistance of $Hf_{0.28}B_{0.72}$ and $Hf_{0.11}Al_{0.20}B_{0.69}$ thin films was investigated comparatively at 700 °C for up to 8 h. Single-phase solid solution thin films were co-sputtered from HfB_2 and AlB_2 compound targets. After oxidation at 700 °C for 8 h an oxide scale thickness of 31 ± 2 nm was formed on $Hf_{0.11}Al_{0.20}B_{0.69}$ which corresponds to 14% of the scale thickness measured on $Hf_{0.28}B_{0.72}$. The improved oxidation resistance can be rationalized based on the chemical composition and the morphology of the formed oxide scales. On $Hf_{0.28}B_{0.72}$ the formation of a porous, O, Hf, and B-containing scale and the formation of crystalline HfO_2 is observed. Whereas on $Hf_{0.11}Al_{0.20}B_{0.69}$ a dense, primarily amorphous scale containing O, Al, B as well as approximately 3 at% of Hf forms, which reduces the oxidation kinetics significantly by passivation. Benchmarking $Hf_{0.11}Al_{0.20}B_{0.69}$ with Ti–Al-based boride and nitride thin films with similar Al concentrations reveals superior oxidation behavior of the Hf-Al-based thin film. The incorporation of few at% of Hf in the oxide scale decelerates oxidation kinetics at 700 °C and leads to a reduction in oxide scale thickness of 21% and 47% compared to $Ti_{0.12}Al_{0.21}B_{0.67}$ and $Ti_{0.27}Al_{0.21}N_{0.52}$, respectively. Contrary to Ti–Al-based diborides, $Hf_{0.11}Al_{0.20}B_{0.69}$ shows excellent oxidation behavior despite B-richness.

Keywords Thin films, Coatings, Borides, High temperature oxidation, $HfAlB_2$, Magnetron sputtering

Transition metal diborides (TMB_2) comprise a combination of covalent-ionic and metallic bonding between B–B, B–TM, and TM–TM[1,2]. Therefore, TMB_2 possess a variety of desirable ceramic-like material properties, such as high hardness[1,3] and elastic modulus[1,4,5], good chemical stability[6,7] and corrosion resistance[8], as well as properties related to the metallic bonding character like high electrical[1] and thermal conductivity[1,4], and relatively large thermal shock resistance compared to other ceramics[9]. The highest oxidation resistance among TMB_2 is reported for HfB_2[10], which belongs with a melting point of 3250 °C[11], to the so-called ultra-high temperature ceramics (UHTC)[1]. Previous research on HfB_2-based materials has therefore focused on high-temperature applications for the aerospace industry, mainly on the HfB_2-SiC system, to increase the heat resistance of structural thermal protection systems to be used as heat shields for re-entry vehicles[9,12,13].

HfB_2 crystallizes—as most TMB_2—in the hexagonal AlB_2 type crystal structure[14] in the space group P6/mmm with lattice constants $a = 3.142$ Å and $c = 3.476$ Å[15]. The AlB_2-type crystal structure is characterized by hexagonal closed-packed layers of TM atoms, with graphite-like atomic sheets of B interspersed between them. This structural arrangement gives rise to the above-discussed combination of covalent-ionic and metallic bonding characters[4,16,17].

Gild et al.[10] compared the oxidation resistance of six different bulk high-entropy transition metal diborides, namely, $(Hf_{0.2}Zr_{0.2}Ta_{0.2}Nb_{0.2}Ti_{0.2})B_2$, $(Hf_{0.2}Zr_{0.2}Ta_{0.2}Mo_{0.2}Ti_{0.2})B_2$, $(Hf_{0.2}Zr_{0.2}Mo_{0.2}Nb_{0.2}Ti_{0.2})B_2$, $(Hf_{0.2}Mo_{0.2}Ta_{0.2}Nb_{0.2}Ti_{0.2})B_2$, $(Mo_{0.2}Zr_{0.2}Ta_{0.2}Nb_{0.2}Ti_{0.2})B_2$, and $(Hf_{0.2}Zr_{0.2}Ta_{0.2}Cr_{0.2}Ti_{0.2})B_2$, to their corresponding,

[1]Materials Chemistry, RWTH Aachen University, Kopernikusstr. 10, 52074 Aachen, Germany. [2]Empa, Swiss Federal Laboratories for Materials Science and Technology, Laboratory for Mechanics of Materials and Nanostructures, Feuerwerkerstrasse 39, 3602 Thun, Switzerland. [3]Plansee Composite Materials GmbH, Siebenbürgerstr. 23, 86963 Lechbruck am See, Germany. [4]Department of Physics and Astronomy, Uppsala University, Lägerhyddsvägen 1, 75120 Uppsala, Sweden. ✉email: kuemmerl@mch.rwth-aachen.de

binary transition metal diborides. Generally, the high-entropy transition metal diborides outperformed the individual binary TMB_2[10]. However, HfB_2 was reported to exhibit a very similar weight gain after oxidation for 1 h at 1000 °C, 1100 °C, and 1200 °C compared to the best-performing high-entropy metal diborides, namely $(Hf_{0.2}Zr_{0.2}Ta_{0.2}Mo_{0.2}Ti_{0.2})B_2$, $(Hf_{0.2}Mo_{0.2}Ta_{0.2}Nb_{0.2}Ti_{0.2})B_2$ and $(Hf_{0.2}Zr_{0.2}Ta_{0.2}Cr_{0.2}Ti_{0.2})B_2$. At 1500 °C HfB_2 outperformed all high-entropy metal diborides underlining its high oxidation resistance[10].

HfB_2 coatings have first been synthesized by chemical vapor deposition and have been studied in terms of wear resistance for tribological applications[18–22]. However, recently chemical composition quantification[23] and oxidation behavior[24] of direct current magnetron sputtered (DCMS) HfB_2 coatings have been reported. Glechner et al.[24] performed oxidation experiments on $Hf_{0.30}B_{0.70}$ in synthetic air with significantly lower water vapor pressure than in ambient air. An increase in mass during dynamic oxidation experiments was observed up to a temperature of 1200 °C, followed by a decrease in mass. This behavior was explained by the evaporation of B_2O_3 above 1200 °C. After 120 min of oxidation at 700 °C, a crystalline oxide containing O, Hf, and B with a scale thickness of 171 ± 21 nm was observed. After oxidation at 800 °C and 900 °C, an additional porous B-rich layer formed on top of a Hf-rich oxide containing O, Hf, and B[24]. However, when oxidation was carried out in ambient air within the same report, no boron oxide was observed which was attributed to the hygroscopic character of B_2O_3 forming volatile compounds[5,24]. Based on secondary ion mass spectrometry (SIMS) data the authors concluded that $Hf_{0.30}B_{0.70}$ films show very limited oxygen inward diffusion (through the scale) and that these films are hence, efficient oxygen diffusion barriers[24].

For bulk samples, it was shown that the oxidation resistance of ZrB_2 and HfB_2 can be improved by the addition of SiC[25–27]. For coatings, it has been demonstrated that the addition of Si into TMB_2 (TM = Ti, Cr, Hf, Ta, W)[28,29] or Al[30] into TiB_2 leads to enhanced oxidation resistance: For $Ti_{0.29}Al_{0.13}B_{0.58}$ a protective Al-containing scale forms during oxidation at 700 °C for up to 8 h which reduced the oxide scale thickness from ~ 1350 nm for the $Ti_{0.29}B_{0.71}$ coating to ~ 460 nm for the $Ti_{0.29}Al_{0.13}B_{0.58}$ coating[30].

Furthermore, the chemical composition and especially the boron-to-metal ratio play a very important role in the oxidation resistance of TMB_2. Under-stoichiometric $Ti_{0.41}B_{0.59}$ (boron-to-metal ratio = 1.4) films have been reported to exhibit superior oxidation resistance compared to over-stoichiometric $Ti_{0.32}B_{0.68}$ and $Ti_{0.27}B_{0.73}$ (boron-to-metal ratio of 2.2 and 2.7 respectively) films due to the absence of the B-tissue phase, resulting in the formation of a denser TiO_x oxide scale with reduced B_2O_3 evaporation, thereby limiting oxide scale growth[31].

One method to deposit stoichiometric Ti–Al–B coatings was shown by Stüber et al.[32] to co-sputter elemental Al to TiB_2 forming a $Ti_{0.84}Al_{0.16}B_{2.0}$ solid solution. Another deposition approach was chosen by Navidi Kashani et al.[33] who studied the effect of the B concentration on the mechanical properties and the oxidation resistance at 700 °C for up to 8 h for Ti–Al–B coatings. Using elemental B targets together with a TiAl target, Ti–Al–B coatings with an Al concentration range of 22 ± 2 at% and varying B concentration from 63 via 67 to 71 at% and hence, above and below stoichiometry, were synthesized. The most favorable combination of the oxidation resistance and mechanical behavior was obtained for the stoichiometric $Ti_{0.12}Al_{0.21}B_{0.67}$ coating with an oxide scale thickness of 39 ± 7 nm. In contrast, the over-stoichiometric $Ti_{0.10}Al_{0.19}B_{0.71}$ coating had a factor 5.2 thicker oxide scale of 204 ± 16 nm after 8 h[33]. Recently, oxidation experiments in ambient air at 700 °C, 800 °C, and 900 °C revealed a strong Al concentration dependence of the oxidation resistance. Stoichiometric films containing ≥ 21 at% of Al formed a dense and passivating oxide scale, while Al concentrations ≤ 15 at% resulted in the formation of a non-passivating scale[34].

Here, we seek to explore, if the oxidation resistance of $Hf_{0.28}B_{0.72}$ thin films can be further improved by Al incorporation. An oxidation temperature of 700 °C was chosen to study the onset of oxidation and compare it with literature data for potential coating materials. To this end, the oxidation resistance and oxide scale formation of $Hf_{0.11}Al_{0.20}B_{0.69}$ is compared to $Hf_{0.28}B_{0.72}$ as well as to the available literature data for Hf-B, Ti–Al–B, and Ti–Al–N films exhibiting similar Al concentrations.

Results and discussion

Sputtering only the HfB_2 target leads to a film with 27.5 ± 3.5 at% Hf, 72.2 ± 3.6 at% B, and 0.3 ± 0.1 at% O according to elastic recoil detection analysis (ToF-ERDA) and will be referred to as $Hf_{0.28}B_{0.72}$ in the following discussion. The B-to-Hf ratio of 2.6 indicates that the film is B over-stoichiometric compared to stoichiometric HfB_2.

This B-richness is in good agreement with other literature reports for DCMS-deposited HfB_x thin films from stoichiometric HfB_2 compound targets[24,35]. The deviation of the film composition from the target composition for constituents with large differences in mass has been proposed to be caused by preferential resputtering of one of the sputtered constituents[36–38] and/or preferential sputtering of the lighter constituent along the target normal[39]. For TiB_x thin films, Neidhardt et al.[40] have demonstrated experimentally and with simulations that there is a complex interaction between the angular distribution of the sputtered flux as well as gas scattering which influences the film composition. The preferential emission of B along the target normal is observed while the angular distribution of Ti is much broader and similar to the ideal spherical cosine distribution. These emission characteristics are modified at higher pressures by the effect of gas scattering. Because of the larger atomic radius, Ti has a more efficient energy transfer with Ar and a shorter thermal mean free path (MFP) than B. This results in more effective stopping and thus less scattering of Ti than B. The complex interdependence between emission characteristics and scattering processescan explain the linear dependence of the Ti/B ratio with pressure and the substrate-to-target distance. As a result, at low pressure, no scattering collisions are expected for B leading to a Ti-deficient film. At high pressures, however, B is scattered preferentially, resulting in a B-deficient film[40]. Mráz et al.[41] studied the angle-resolved thin film composition evolution during sputtering of a Cr_2AlC compound target by varying the angle α between the target normal and the substrate surface between 0° and 67.5°. As the mass differences in this system are larger than for TiB_2, significant differences between film and target composition were reported: for $\alpha \leq 22.5°$heavy element deficient thin films compared to the target composition are observed

where the deficiency decreases with increasing pressure. However, this heavy element deficiency is decreasing with increasing angle between the target normal and the substrate surface[41].

In $Hf_{0.28}B_{0.72}$ the mass difference between the target constituents is larger and $\alpha = 0°$. Hence, the angular distribution of Hf and B differs more severely than in TiB_2[40] and the formation of Hf-deficient thin films is expected based on the reasoning in[40] and[41].

To estimate the effect of gas phase scattering the MFP was calculated using Eq. (1) which includes the deposition temperature ($T = 673$ K), deposition pressure ($p = 0.6$ Pa), covalent radii of Ar ($r_{Ar} = 71$ pm[42]), Hf ($r_{Hf} = 208$ pm[42]) or B ($r_B = 87$ pm[42]).

$$MFP = \frac{1}{\sqrt{2}} \frac{k_B T}{p} \frac{1}{\pi (r_{Ar} + r_{Hf,B})^2} \tag{1}$$

The MFP of B is 14.0 cm leading at a substrate-to-target distance of 10 cm to an average number of 0.7 collisions. An average of < 1 collision implies that B atoms will likely not undergo collisions on route to the target and will therefore likely be incorporated in the growing thin film. In contrast, the MFP of Hf is 4.5 cm resulting in 2.2 collisions on average, causing less efficient transport of Hf to the surface of the growing film which is in turn leading to a Hf-deficient and hence B-rich thin film[40]. Therefore, the here observed Hf deficiency (compared to the target composition) can be attributed to preferential emission of B along the target normal as well as efficient scattering of Hf.

When AlB_2 is co-sputtered with HfB_2 at the same angle α between the target normal and the substrate surface, the B over-stoichiometry decreases to a B/(Hf + Al) ratio of 2.3 which corresponds to 69.2 ± 3.5 at% B and Al and Hf concentrations of 19.8 ± 2.2 at% and 10.5 ± 1.2 at%, respectively. Henceforth, the film will be referred to as $Hf_{0.11}Al_{0.20}B_{0.69}$. The oxygen concentration was 0.5 ± 0.1 at%. The reduced B over-stoichiometry compared to $Hf_{0.28}B_{0.72}$ can be explained by the smaller mass ($m_{Al} = 26.98$ u) and atomic radius ($r_{Al} = 118$ pm[42]) of Al compared to Hf with $m_{Hf} = 178.49$ u and $r_{Hf} = 208$ pm[42], which leads to an MFP of 9.8 cm and therefore to an average number of 1.0 collisions and thus to more efficient Al transport towards the surface of the growing film. Hence, as more metal is incorporated into the film the B-richness is reduced.

Figure 1 depicts X-ray diffraction (XRD) patterns of the as-deposited films grown on α-Al_2O_3 (0001) to investigate the phase formation. The positions of HfB_2 and AlB_2 reference lines according to the JCPDS cards 00-038-1398 and 00-008-0216 are highlighted with circle and triangle markers, respectively. The diffractogram of $Hf_{0.28}B_{0.72}$ reveals the formation of a single-phase hexagonal HfB_2 structure. The peak positions of the $Hf_{0.11}Al_{0.20}B_{0.69}$ films are located between those of the binary HfB_2 and AlB_2 phases, indicating the formation of a solid solution. Based on our DFT data this solid solution is metastable as witnessed by the positive mixing enthalpy of 0.08 eV/atom for stoichiometric $Hf_{0.12}Al_{0.21}B_{0.67}$.

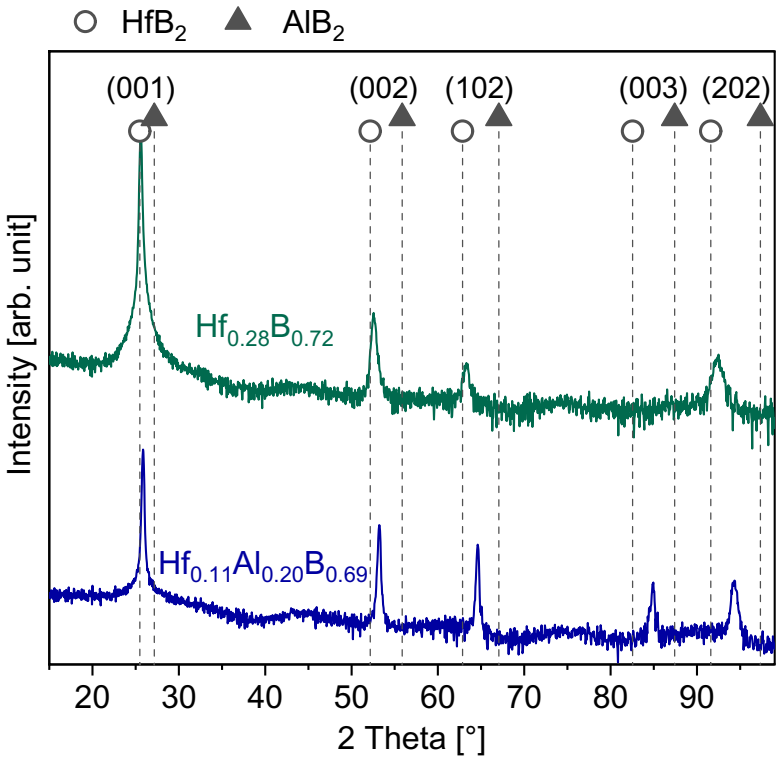

Fig. 1. Diffraction patterns of as-deposited $Hf_{0.28}B_{0.72}$ and $Hf_{0.11}Al_{0.20}B_{0.69}$ thin films.

Figure 2 shows the calculated and experimentally obtained lattice constants *a* and *c* as a function of Al concentration *x* in $Hf_{0.33-x}Al_xB_{0.67}$. While the calculated lattice constant *a* decreases almost linearly with the Al concentration following Vegard´s law[43], the *c* parameter exhibits a non-linear behavior. The deviation of the experimental to the density functional theory (DFT) calculated lattice parameter of $Hf_{0.28}B_{0.72}$ is − 0.3% for *a* and − 0.8% for *c* and of $Hf_{0.11}Al_{0.20}B_{0.69}$ it is + 0.9% for *a* and − 0.6% for *c*, respectively. According to Paier et al., deviations of up to 2.1% between DFT-calculated and experimental lattice parameters have to be expected based on the here-applied exchange–correlation functionals[44]. Hence, very good agreement between prediction and experiment is obtained even though the B over-stoichiometry and the actual stress state of the as-deposited thin films were not considered.

To study the morphology, cross-sectional and plan view scanning transmission electron microscopy (STEM) images in bright-field (BF) mode were taken which are shown in Fig. 3. $Hf_{0.28}B_{0.72}$ exhibits a small-grained, dense, and nanocolumnar microstructure. While this observation is consistent with literature reports from Mayrhofer et al.[3] where the excess boron is reported to surround the columns and between smaller sub-columns, the formation of a B-rich tissue phase cannot be inferred from the images presented here.

The ternary solid solution film also shows a dense, columnar morphology; however, the column size is increased as depicted in Fig. 3b,d compared to Fig. 3a,c. The hardness and elastic modulus determined for the $Hf_{0.28}B_{0.72}$ film are 38 ± 2 GPa and 541 ± 19 GPa, respectively, which is reduced to 30 ± 1 GPa and 397 ± 9 GPa after Al addition forming $Hf_{0.11}Al_{0.20}B_{0.69}$. As depicted in Fig. 2, the elastic modulus of $Hf_{0.28}B_{0.72}$ matches the values predicted by DFT within the error bar. The experimentally determined elastic modulus of $Hf_{0.11}Al_{0.20}B_{0.69}$ is 18.5% higher than the DFT calculated value of 334 GPa, which is according to Paier et al.[44] within the expected range of bulk modulus deviations between different exchange–correlation functionals and experiments. As the Al concentration is increased from 0 at% via 20 at% to 33 at% in $Hf_{0.33-x}Al_xB_{0.67}$, the cohesive energy increases linearly from − 7.87 eV/atom via − 6.44 eV/atom to − 5.68 eV/atom, respectively. The increase in cohesive energy indicates that the reduction in elastic modulus can be explained by bond weakening caused by Al addition as observed in $Ti_{0.33-x}Al_xB_{0.67}$[34]. This bond weakening leads to an elastic modulus reduction of ~ 7 GPa per at% of Al in $Hf_{0.33-x}Al_xB_{0.67}$. Al concentration induced bond weakening has also been reported for $Ti_{0.33-x}Al_xB_{0.67}$, where also a ~ 7 GPa reduction was observed for each at% Al added[34].

The time-dependent oxidation resistance at 700 °C of the ternary solid solution $Hf_{0.11}Al_{0.20}B_{0.69}$ thin film was compared to the binary $Hf_{0.28}B_{0.72}$ thin film. In Fig. 4 the diffractograms of the as-deposited and oxidized films after 4 and 8 h are presented. The positions of HfO_2 reference lines according to the JCPDS card 01-070-2832 is shown by the square marker in addition to the positions of AlB_2 and HfB_2 from Fig. 1. It is evident that for $Hf_{0.28}B_{0.72}$ crystalline HfO_2 is formed between 4 and 8 h of oxidation. In contrast, for $Hf_{0.11}Al_{0.20}B_{0.69}$ no additional diffraction signals are visible, even after 8 h of oxidation, indicating the absence of X-ray crystalline oxide scales.

Figure 5 shows a high angle annular dark field (HAADF) high-resolution STEM (HRSTEM) micrograph along with corresponding energy dispersive X-ray spectroscopy (EDX) maps and line scans capturing the oxide scale including the interfacial region as well as the underlying unaffected thin film for oxidized $Hf_{0.28}B_{0.72}$ and $Hf_{0.11}Al_{0.20}B_{0.69}$ after 8 h at 700 °C. It should be noted that due to the difference in oxide scale thickness of $Hf_{0.28}B_{0.72}$ and $Hf_{0.09}Al_{0.21}B_{0.70}$, the scale bars in the images and the corresponding EDX maps differ.

The HAADF image of $Hf_{0.28}B_{0.72}$, see Fig. 5a, shows a bi-layered oxide scale morphology, where the ~ 100 nm thick top layer is more porous than the ~ 160 nm thick layer below. The corresponding EDX line scan and maps indicate the formation of an O, Hf, and B-containing oxide. The B concentration gradually decreases while the Hf concentration increases from the oxide surface towards the film. The fact that Pt, utilized during lamellae preparation, was able to penetrate the oxide scale could amplify the decrease in the Hf concentration measured in the line scan. Furthermore, literature shows that B quantification in TEM–EDX spectra is strongly affected by the lamellae thickness due to preferential B-K_α X-ray absorption with increasing film thickness[45]. Hence, we

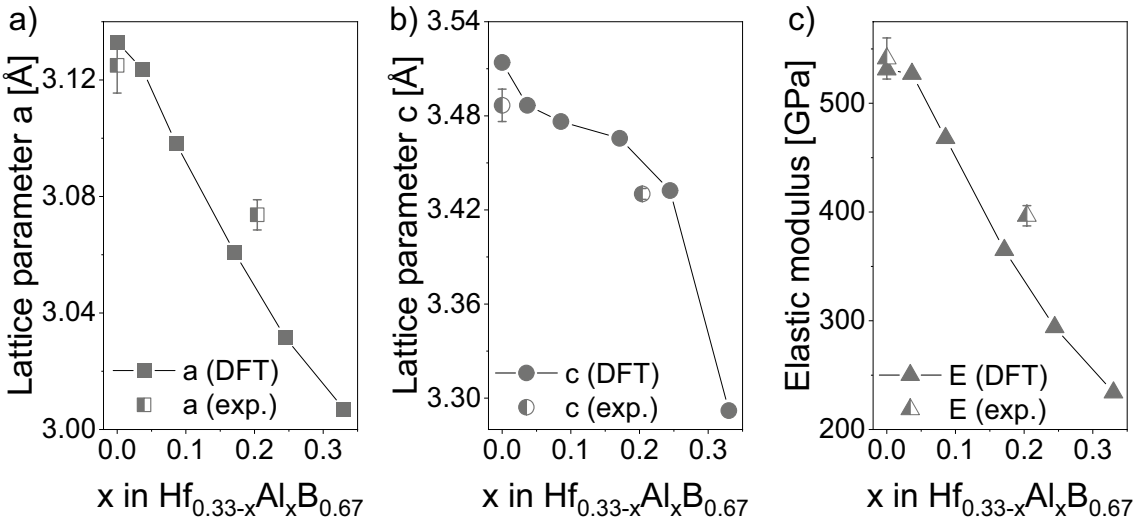

Fig. 2. Change in lattice parameters (**a**) a and (**b**) c as well as (**c**) the elastic modulus as a function of the Al concentration x in $Hf_{0.33-x}Al_xB_{0.67}$ calculated by DFT and compared with experimental data.

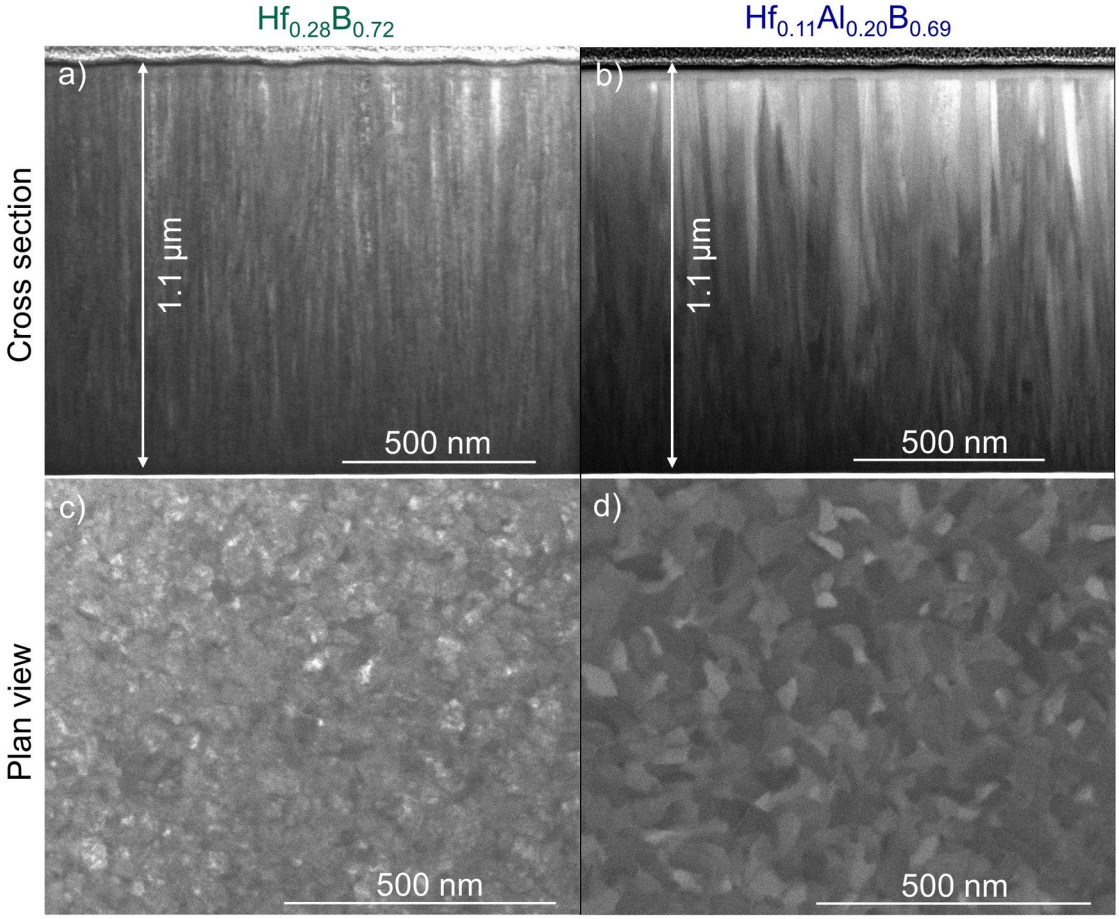

Fig. 3. STEM images of as-deposited $Hf_{0.28}B_{0.72}$ (**a** and **c**) and $Hf_{0.11}Al_{0.20}B_{0.69}$ (**b** and **d**) thin films in BF-mode from cross-sectional (**a** and **b**) and plan view (c and d).

assume that the increasing lamellae thickness towards the substrate is causing the above-discussed composition variations.

Similar to the present study, Glechner et al.[24] reported a bi-layered oxide scale formation for $Hf_{0.30}B_{0.70}$ thin films oxidized in synthetic air, with a B-rich surface-near oxide layer and a Hf-rich oxide layer underneath based on SIMS data. However, the porous boron oxide layer was based on electron microscopy cross-sections only described for $Hf_{0.30}B_{0.70}$ thin films oxidized above 800 °C and the boron oxide on the surface only for synthetic air experiments. When the experiment was repeated in ambient air, no boron oxide was found on the surface which was explained by the formation of volatile H_mBO_n in the presence of water vapor which evaporates earlier. However, there is no detailed description of the composition and morphology of the oxide scale at 700 °C for the oxidation experiment conducted in ambient air[24].

In this study, after oxidation at 700 °C for 8 h, the formation of crystalline HfO_2 is detected by XRD concurrent with EDX which indicates that the oxide scale consists of O, Hf, and B, while the HRSTEM image shows a porous morphology. Based on the oxidation model for bulk HfB_2 from Parthasarathy et al.[46], for oxidation temperatures < 1000 °C a glassy B_2O_3 film is expected to form on top of a porous, crystalline HfO_2 scale, where the pores are filled with B_2O_3. At temperatures > 1000 °C B_2O_3 at the surface starts to evaporate[46].

However, experiments and thermodynamic calculations with water-saturated synthetic air, with a water vapor pressure of 0.031 atm at 25 °C, showed that in the presence of water vapor B_2O_3 reacts and forms hydrated B–O compounds like HBO_2 and H_3BO_3 which evaporate below 1000 °C[5,47].

There are opposing reports in the literature about the rate of B_2O_3, or more specifically H_mBO_n evaporation, at ~ 700 °C in ambient air. Some authors report an almost complete absence of the B_2O_3 phase for Ti-B films oxidized in synthetic air with 40% humidity[47] and Hf-B films oxidized in ambient air[24]. However, there are also reports of the presence of B_2O_3 in the oxide scale forming on TiB_2 bulk samples oxidized in ambient air at this temperature[48] or even at 1200 °C for 1 h of oxidation of ZrB_2 bulk samples oxidized in water-saturated synthetic air[5]. This suggests that a Hf and B containing oxide scalesimilar to the oxidation model for bulk HfB_2 has formed on the here investigated $Hf_{0.28}B_{0.72}$ where some B_2O_3 has started to form H_mBO_n and thus has evaporated leaving pores in the oxide scale in the vicinity of the surface. However, also here the discussed limitation in B quantification for films with decreasing thickness applies[45]. Therefore, we conclude that based on the EDX and TEM results, a Hf-B containing oxide scale has formed where some B has formed volatile H_mBO_n and evaporated leaving pores. Still, significant amounts of B are still present in the scale after oxidation at 700 °C for 8 h.

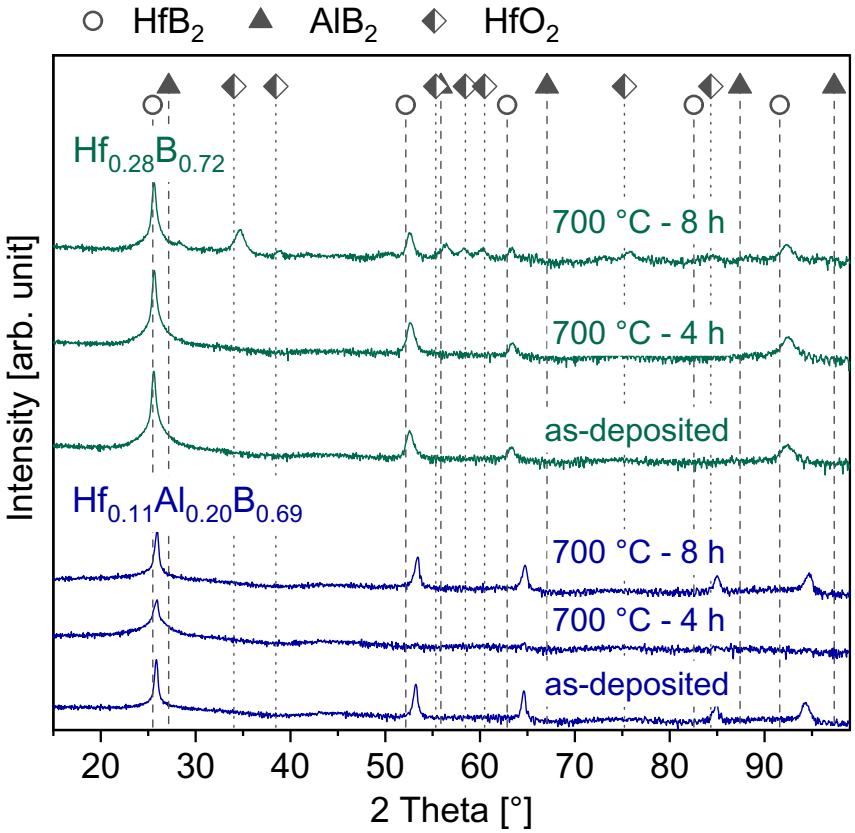

Fig. 4. Diffraction patterns of as-deposited and oxidized $Hf_{0.28}B_{0.72}$ and $Hf_{0.11}Al_{0.20}B_{0.69}$ thin films at 700 °C.

The oxide scale forming on $Hf_{0.11}Al_{0.20}B_{0.69}$ is dense and contains besides O also equal amounts of Al and B as well as approximately 3 at% of Hf. The EDX maps show that the elements are homogeneously distributed. Based on ERDA measurements, the O concentration in the remaining film is below 1 at% and thus significantly lower than the ~ 18 at% O concentration measured by EDX. This observation can be explained by the sample preparation procedure. For the HRSTEM EDX analysis, a ~ 60 nm thin lamella is prepared in the focused ion beam (FIB) and subsequently transferred through ambient air. Thus, it is reasonable to assume that oxidation by atmosphere exposure causes the formation of native oxides on each side of the lamella, which will affect the measured amount of O in EDX. Therefore, the $Hf_{0.28}B_{0.72}$ film exhibits ~ 10 at% of O. The 8 at% higher O content in $Hf_{0.11}Al_{0.20}B_{0.69}$ might be related to the higher Al concentration in the film.

Moreover, EDX is not well positioned to quantify the boron content, since light elements have low characteristic X-ray energies and a low yield resulting in difficulties in accurate resolution of their signals against background noise and limitations in detector sensitivity[49]. As a consequence, the accuracy of boron concentration measurements obtained by EDX is limited, and previous studies have reported systematic overestimation of boron concentration in Hf-B thin films using this technique when compared to ERDA[23]. Nevertheless, from the here obtained HRSTEM and EDX data it is evident that $Hf_{0.11}Al_{0.20}B_{0.69}$ forms a dense oxide scale containing around 30 at% of Al and B as well as 3 at% of Hf, as determined within the known limitations of EDX.

Based on XRD the oxide forming on $Hf_{0.11}Al_{0.20}B_{0.69}$ is amorphous. Transmission electron microscopy (TEM) dark field (DF) images of the interface between the oxide scale and film, which are depicted in Fig. 6, also show a mostly amorphous oxide scale. However, nanocrystalline regions, marked with red arrows, are visible preferentially in the vicinity of the interface which may have formed during oxidation or electron beam exposure. The unoxidized film is crystalline and the interface between oxide and film is well defined.

To study the oxide growth kinetics, Fig. 7 shows the resulting oxide scale thicknesses of the film determined by STEM imaging on FIB-prepared lamellae as a function of oxidation time at 700 °C. Also, the relevant literature data, namely magnetron sputtered $Hf_{0.30}B_{0.70}$[24], $Ti_{0.12}Al_{0.21}B_{0.67}$[33], $Ti_{0.10}Al_{0.19}B_{0.71}$[33], and $Ti_{0.27}Al_{0.21}N_{0.52}$[34] thin films, are added for comparison. After 1 h of oxidation at 700 °C, $Hf_{0.28}B_{0.72}$ exhibits an oxide layer thickness of 45 ± 4 nm. During further oxidation, this thickness increases significantly from 89 ± 3 nm after 4 h to 216 ± 14 nm after 8 h. Oxidation of $Hf_{0.11}Al_{0.20}B_{0.69}$ at 700 °C after 1 h results in the formation of a 22 ± 1 nm thick oxide layer, which increases to 30 ± 1 nm and 31 ± 2 nm after 4 and 8 h, respectively.

To study the oxidation behavior and the effect of the Al addition on the oxidation kinetics, a power law fit according to[50] was utilized.

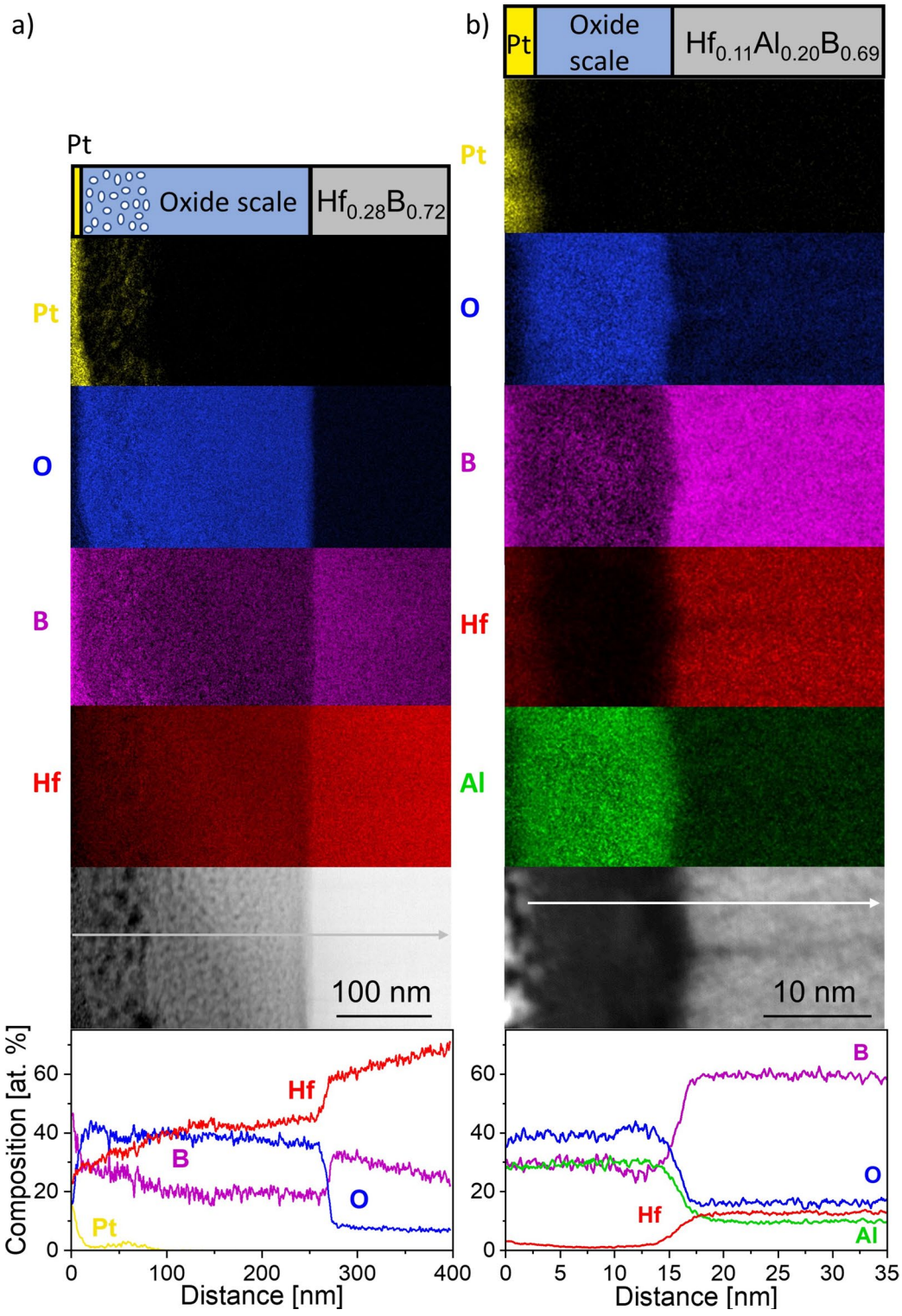

Fig. 5. HRSTEM EDX line scans, EDX maps, and a HAADF cross-section image of the oxidized (**a**) $Hf_{0.28}B_{0.72}$ and (**b**) $Hf_{0.11}Al_{0.20}B_{0.69}$ after 8 h at 700 °C, where the grey arrows mark the positions of the line scans.

$$\Delta x = K' \left(\frac{t}{t_0} \right)^n \tag{2}$$

The oxide scale thickness Δx is measured in μm, $t_0 = 1s$, t is the oxidation time measured in seconds, K' is the pre-exponential factor and n is the time exponent, where exponents of 0.5 and 0.33 would indicate parabolic

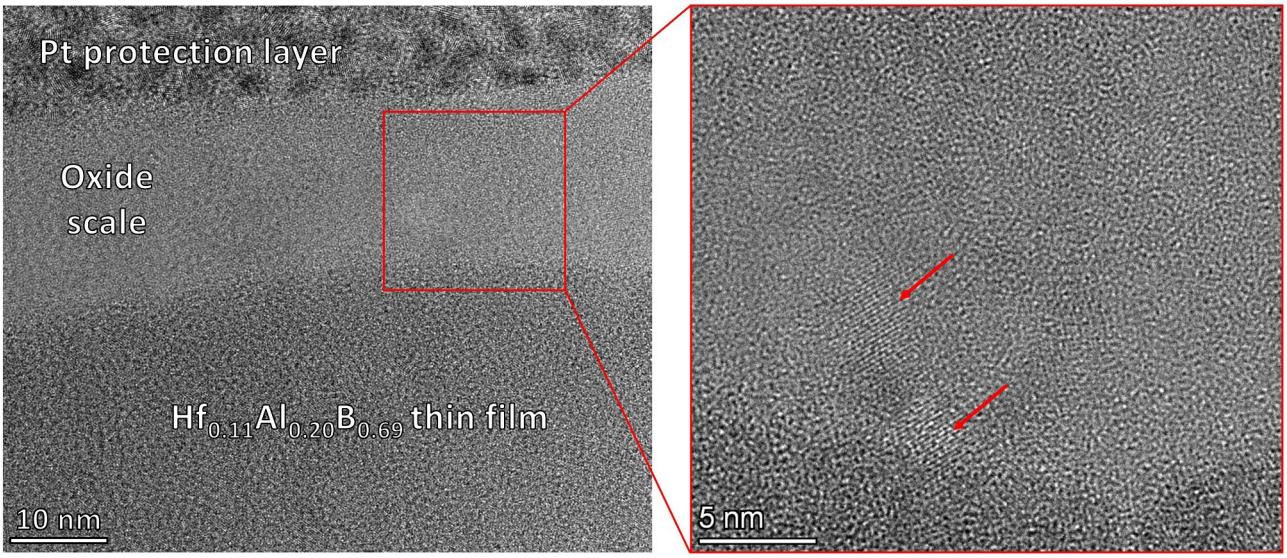

Fig. 6. Typical cross-sectional DF TEM image of the oxide scale of $Hf_{0.11}Al_{0.20}B_{0.69}$. The red arrows mark the nanocrystalline areas.

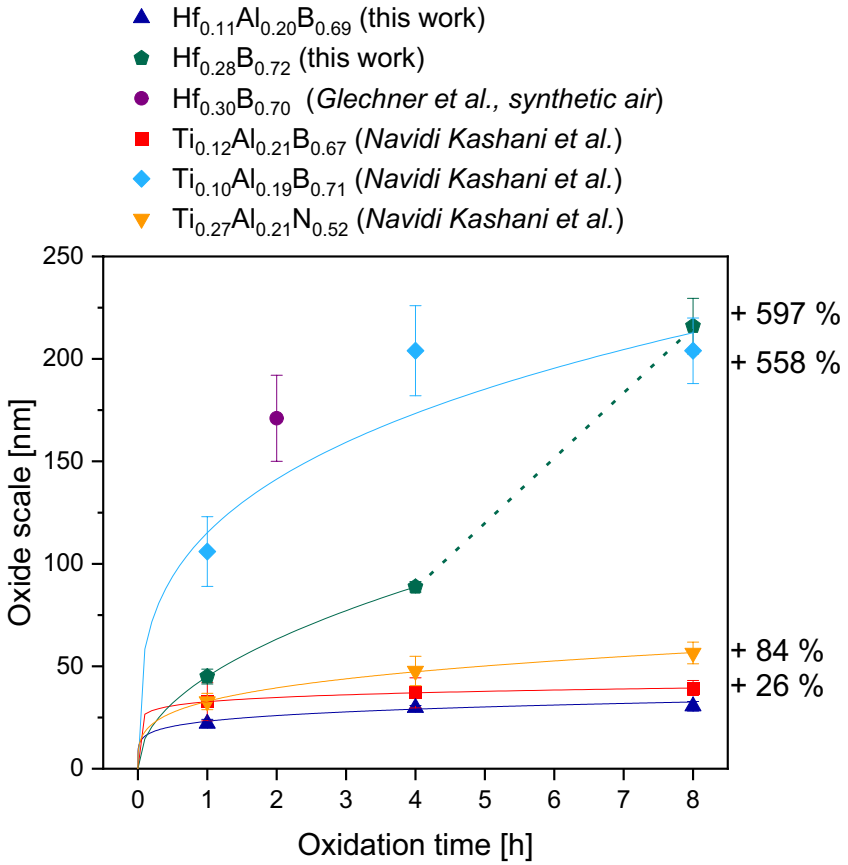

Fig. 7. Oxide scale thickness as a function of oxidation time at 700 °C for $Hf_{0.28}B_{0.72}$ and $Hf_{0.11}Al_{0.20}B_{0.69}$ compared to the available literature data from Glechner et al.[24] and Navidi Kashani et al.[33,34]. The dashed line for $Hf_{0.28}B_{0.72}$ is included as a guide for the eye.

and cubic oxidation kinetics, respectively. The pre-exponential factor K' and the time exponent n determined for the films compared in Fig. 7 are listed in Supplementary Table 1.

Initially, the $Hf_{0.28}B_{0.72}$ thin film shows a parabolic oxidation behavior with n = 0.49. During that initial state, no oxide peaks occur in XRD diffractograms, indicating the formation of an X-ray amorphous Hf and B containing oxide scale. However, beyond 4 h of oxidation at 700 °C, the oxide scale crystallizes and pore formation in the oxide scale increases leading to the acceleration of oxidation kinetics as indicated by the dashed line to guide the eye and thus a non-passivating behavior. The observation that $Hf_{0.29}B_{0.71}$ shows initially slow oxidation kinetics at 700 °C which then increases after a certain time has been reported previously[24].

In contrast, $Hf_{0.11}Al_{0.20}B_{0.69}$ shows with n = 0.16 a much slower, sub-cubic oxidation rate. The substantially improved oxidation resistance of $Hf_{0.11}Al_{0.20}B_{0.69}$ compared to $Hf_{0.29}B_{0.71}$ can be rationalized based on the XRD, EDX, HRSTEM and TEM data: firstly, the morphologies of the formed oxides vary significantly: While on $Hf_{0.29}B_{0.71}$ the formation of a porous, crystalline oxide scale is observed, oxidation of $Hf_{0.11}Al_{0.20}B_{0.69}$ results in a dense, amorphous and passivating oxide scale. Secondly, the chemical composition of the oxide varies significantly: while $Hf_{0.29}B_{0.71}$ forms a Hf-rich oxide scale containing significant amounts of B, $Hf_{0.11}Al_{0.20}B_{0.69}$ forms an oxide scale with only small amounts of Hf but high Al and B concentration.

Next, the influence of the transition metal on the oxidation resistance is discussed by comparing $Hf_{0.09}Al_{0.21}B_{0.70}$ with over-stoichiometric $Ti_{0.10}Al_{0.19}B_{0.71}$ and stoichiometric $Ti_{0.12}Al_{0.21}B_{0.67}$[33]. It is evident from Fig. 7 that $Ti_{0.12}Al_{0.21}B_{0.67}$ and $Hf_{0.11}Al_{0.20}B_{0.69}$ show a similar oxidation behavior, however, the oxide thickness of $Ti_{0.12}Al_{0.21}B_{0.67}$ is 26% thicker than for $Hf_{0.11}Al_{0.20}B_{0.69}$ after 8 h of oxidation. It is noteworthy that the here investigated $Hf_{0.11}Al_{0.20}B_{0.69}$ is both, over-stoichiometric with a boron-to-metal ratio of 2.2 and superior in oxidation behavior compared to stoichiometric $Ti_{0.12}Al_{0.21}B_{0.67}$. As pointed out in the introduction the boron-to-metal ratio plays a major role in the oxidation resistance of Ti–Al–B thin films as a comparison with the over-stoichiometric $Ti_{0.10}Al_{0.19}B_{0.71}$[33] illustrates. The over-stoichiometric $Ti_{0.10}Al_{0.19}B_{0.71}$ thin film shows an increase in oxide scale thickness by factor 5.2 resulting in 204 ± 16 nm compared to stoichiometric $Ti_{0.12}Al_{0.21}B_{0.67}$ after oxidation at 700 °C for 8 h. The reason is the formation of a porous oxide scale, which is enriched in Ti and O as well as depleted in Al and B and is therefore less oxidation resistant. In contrast, the stoichiometric $Ti_{0.12}Al_{0.21}B_{0.67}$ film forms a dense, Al-rich oxide scale which is highly oxidation resistant[33] as a passivating scale is formed[34]. The $Hf_{0.11}Al_{0.20}B_{0.69}$ film shows excellent oxidation resistance even though a significant amount of B is in the Al-rich oxide scale.

Another advantage of $Hf_{0.11}Al_{0.20}B_{0.69}$ compared to Ti–Al–B films with a similar Al concentration[33] is the enhancement of mechanical properties. The highly oxidation-resistant $Ti_{0.12}Al_{0.21}B_{0.67}$ exhibits hardness and elastic modulus values of 19 ± 1 GPa and 395 ± 12 GPa, respectively. The elastic modulus is similar to the $Hf_{0.11}Al_{0.20}B_{0.69}$ film, however, the hardness is significantly reduced compared to 30 ± 1 GPa of $Hf_{0.11}Al_{0.20}B_{0.69}$. Higher hardness is observed for the over-stoichiometric $Ti_{0.10}Al_{0.19}B_{0.71}$ with 24 ± 1 GPa, but still significantly lower than for $Hf_{0.11}Al_{0.20}B_{0.69}$. Moreover, the elastic modulus of over-stoichiometric $Ti_{0.10}Al_{0.19}B_{0.71}$ is only 330 ± 9 GPa, and the oxidation resistance is much inferior with an oxide scale thickness that is 558% larger than the one of $Hf_{0.11}Al_{0.20}B_{0.69}$[33].

Finally, $Hf_{0.11}Al_{0.20}B_{0.69}$ is compared to the industrial benchmark coating $Ti_{0.27}Al_{0.21}N_{0.52}$[34]. After oxidation at 700 °C for 8 h, the nitride film exhibits an oxide scale thickness of 57 ± 5 nm corresponding to an 84% increased thickness compared to $Hf_{0.11}Al_{0.20}B_{0.69}$. This data shows that $Hf_{0.11}Al_{0.20}B_{0.69}$ exhibits superior combined mechanical and oxidation behavior at 700 °C compared to Ti–Al-based diborides and nitrides, even when the boron-to-metal ratio is over-stoichiometric. The fact that the oxidation resistance of Hf-Al-based diborides, in contrast to Ti–Al-based diborides, is not adversely affected by over-stoichiometric B concentrations results in less stringent requirements concerning the composition distribution obtained within an industrial deposition system.

Conclusion

Single-phase solid solution $Hf_{0.29}B_{0.71}$ and $Hf_{0.11}Al_{0.20}B_{0.69}$ thin films with a hexagonal crystal structure were synthesized by magnetron sputtering to investigate the phase formation and oxidation behavior of Hf-Al-B thin films for the first time. DFT calculations of the mixing enthalpy of Hf-Al-B predict a metastable solid solution and the DFT-calculated lattice parameters are in very good agreement with the experimentally obtained lattice parameters a and c.

$Hf_{0.29}B_{0.71}$ thin films exhibit a hardness of 38 ± 2 GPa and an elastic modulus of 541 ± 19 GPa. The addition of Al, forming $Hf_{0.11}Al_{0.20}B_{0.69}$, leads to a reduction in hardness and elastic modulus to 30 ± 1 GPa and 397 ± 9 GPa, respectively. Both experimentally determined elastic modulus values are in good agreement with DFT predictions and can be understood by considering the corresponding changes in cohesive energy showing Al concentration induced bond weakening. After isothermal oxidation at 700 °C for 8 h of $Hf_{0.29}B_{0.71}$, an oxide scale thickness of 216 ± 14 nm was obtained. When $Hf_{0.11}Al_{0.20}B_{0.69}$ was oxidized under the same conditions the oxide scale thickness was 31 ± 2 nm, which corresponds to an 86% reduction compared to $Hf_{0.29}B_{0.71}$. This behavior can be explained by comparing the chemical composition and the morphology of the corresponding oxide scales. While on $Hf_{0.29}B_{0.71}$ a porous, O, Hf, and B-containing scale is formed with crystalline HfO_2 peaks observed by XRD, on $Hf_{0.11}Al_{0.20}B_{0.69}$ a dense, predominantly amorphous scale containing O, Al, B as well as small amounts of Hf is formed, which reduces the oxidation kinetics significantly by passivation.

While B over-stoichiometry leads to a deterioration in oxidation behavior in Ti–Al-based diborides[31,33], B-rich $Hf_{0.11}Al_{0.20}B_{0.69}$ shows sub-cubic oxidation kinetics similar to stoichiometric $Ti_{0.12}Al_{0.21}B_{0.67}$[33]. As a result, the oxide layer thickness of $Ti_{0.10}Al_{0.19}B_{0.71}$ is 558% thicker compared to $Hf_{0.11}Al_{0.20}B_{0.69}$, because $Hf_{0.11}Al_{0.20}B_{0.69}$ exhibits an oxide scale that is denser and less enriched in the transition metal than the scale of $Ti_{0.10}Al_{0.19}B_{0.71}$[33]. A comparison of $Hf_{0.11}Al_{0.20}B_{0.69}$ and $Ti_{0.12}Al_{0.21}B_{0.67}$[33] thin films shows that despite the B over-stoichiometry in $Hf_{0.11}Al_{0.20}B_{0.69}$, $Ti_{0.12}Al_{0.21}B_{0.67}$ exhibits a 26% thicker oxide scale, indicating that the O diffusion through the

Al_2O_3 and B_2O_3 containing oxide scale is slowed down by the incorporation of approximately 3 at% of Hf even if the B concentration in the $Hf_{0.11}Al_{0.20}B_{0.69}$ oxide scale seems to be larger than for $Ti_{0.12}Al_{0.21}B_{0.67}$. $Hf_{0.11}Al_{0.20}B_{0.69}$ outperforms well-established $Ti_{0.27}Al_{0.21}N_{0.52}$[33] regarding oxidation behavior since the oxide scale thickness of the nitride is 84% thicker than on $Hf_{0.11}Al_{0.20}B_{0.69}$.

This study highlights the untapped application potential of Hf-Al-based diboride thin films for oxidation protection. Very significantly, in comparison to Ti–Al-based diborides, Hf-Al-based diborides have the advantage of forming passivating oxide scales for B-rich thin film compositions, thereby improving processability while exhibiting a high hardness of 30 ± 1 GPa.

Methods

Experimental methods

The $Hf_{0.28}B_{0.72}$ and $Hf_{0.11}Al_{0.20}B_{0.69}$ thin films were synthesized by direct current magnetron sputtering using an in-house built high-vacuum growth system with a base pressure of less than 6×10^{-4} Pa at the deposition temperature of 400 °C. Stoichiometric 2-inch HfB_2 (99.8% purity) and AlB_2 (99.8% purity) compound targets (Plansee Composite Materials GmbH) were mounted at a 45° angle with respect to the substrate normal as depicted in Supplementary Fig. 1.

For the $Hf_{0.11}Al_{0.20}B_{0.69}$ deposition, the HfB_2 and AlB_2 targets were co-sputtered at a constant power density of 3.9 W/cm^2 and 7.4 W/cm^2, respectively. To deposit the reference $Hf_{0.28}B_{0.72}$ thin film only the HfB_2 target was operated at a constant power density of 7.4 W/cm^2. All films were grown in pure Ar atmosphere (99.9999% purity) at 0.6 Pa and floating substrate bias potential onto 10×10 mm^2 α-Al_2O_3 (0001) substrates with a target-to-substrate distance of 10 cm. Substrate rotation was used to ensure a homogenous composition. The deposition time was chosen so both film thicknesses were 1 µm with deposition rates of 13.3 nm/min for $Hf_{0.11}Al_{0.20}B_{0.69}$ and 11.1 nm/min for $Hf_{0.28}B_{0.72}$.

The samples were oxidized in ambient air at 700 °C for exposure times of 1, 4, and 8 h using a GERO tube furnace. The as-deposited samples were placed into an Al_2O_3 crucible with an attached Ni/Ni–Cr thermocouple and transferred into the pre-heated furnace at 700 °C and immediately removed from the furnace after the exposure time.

For the structural analysis, a Bruker AXS D8 Discover General Area Detector Diffraction System was used where the Cu K_α ($\lambda = 1.5406$ Å) X-ray source was set to 40 kV at a current of 40 mA and the incident angle was fixed at 15°. The peaks were fitted with a pseudo-Voigt II function using the TOPAS software V.3. Based on the fitted peak positions, lattice parameters were calculated using the CellCalc software V. 2.10.

For determining the chemical composition, time-of-flight elastic recoil detection analysis (ToF-ERDA) was carried out at the Tandem Accelerator Laboratory of Uppsala University [https://doi.org/https://doi.org/10.1088/1748-0221/17/04/P04011]. Recoils were generated using a 36 MeV $^{127}I^{8+}$ primary ion beam and time-energy coincidence spectra were recorded with a detector telescope, equipped with thin carbon foils for ToF measurement and a gas detector for energy discrimination[51]. Further information on the detector telescope and the ToF setup is available in reference[52]. Uncertainties regarding the stopping power values as well as the detection efficiency dominate the measurement uncertainty[53] and beam straggling and multiple scattering diminish the depth resolution for heavy transition metals like Hf[54]. For Ti-B films it has been reported that ERDA and Rutherford backscattering spectrometry deviate less than 3% and thus coincide very well[23]. Since ERDA is employed as a stand-alone technique in the present work, a maximum total uncertainty of 5% of the deduced values is assumed for the light element B and aliquot fractions thereof for the metals (Hf,Al). The composition was quantified from the surface near region of the depth profile to prevent an influence of multiple scattering on the chemical composition analysis[23,54,55].

The mechanical properties of as-deposited films were determined by quasistatic nanoindentation in a Hysitron TI-900 TriboIndenter. Indentation modulus as well as hardness were derived according to the method from Oliver and Pharr[56]. A diamond indenter (Poisson's ratio of 0.07, elastic modulus of 1140 GPa) with Berkovich geometry was used. Load-controlled measurements with 6 mN were applied, resulting in maximum contact depths of 60 nm for as-deposited samples, corresponding to < 6% of the film thickness. 50 indents were performed for each sample and the indenter area function was derived from measurements on fused silica. Measured indentation modulus values were converted to the elastic modulus with a Poisson's ratio of 0.154 for HfB_2, obtained by averaging published data from density functional theory (DFT) calculations[57–60]. For $Hf_{0.11}Al_{0.20}B_{0.69}$ a Poisson's ratio of 0.131 was used, based on the interpolation between HfB_2 and the calculated value of 0.118 for AlB_2[34].

Scanning transmission electron microscopy (STEM) was performed to study the microstructure of as-deposited and oxidized samples in a dual-beam microscope FEI Helios NanoLab 600 with a Ga^+ focused ion beam (FIB) and equipped with an EDAX Octane Elect energy dispersive X-ray spectroscopy (EDX) detector. First, the lamellae were prepared with a standard lift-out procedure, and then STEM imaging was carried out at an acceleration voltage of 30 kV and a current of 50 pA.

Transmission electron microscopy (TEM) was utilized to study the microstructure and chemical composition using a Thermo Fisher Scientific Titan Themis 200 G3 equipped with a SuperX detector for EDX mapping. The TEM lamellae were first prepared in the FEI Helios NanoLab 600 as well and were subsequently thinned and polished at 5 kV using a Tescan Lyra FIB/SEM system.

Computational methods

The lattice constants of relaxed $Hf_{0.33-x}Al_xB_{0.67}$ with $x = 0$, 0.04, 0.09, 0.17, 0.24, and 0.33 were calculated based on DFT[61,62] as implemented in the Vienna ab initio simulation package (VASP)[63,64]. The projector augmented-plane-wave method[65,66] was used with the generalized gradient approximation with PBE[67] functional described the exchange–correlation effects. The plane-wave cutoff energy was set to 500 eV, and a $7 \times 7 \times 7$ k-point mesh

was used. For the calculations, 3 × 3 x 3 supercells of the AlB_2-type (P6/mmm) were created. The metal sublattice was populated with Hf and Al using the Special Quasi-random Structures method as implemented in[68]. The X-ray diffraction (XRD) patterns from the calculated structures were determined with the VESTA software[69]. The elastic constants were calculated in the form of the full stiffness tensor (C_{ij}), from which the Young's modulus was derived with the Voigt-Reuss-Hill scheme[70]. The stiffness tensor was obtained with the strain–stress method[71].

Data availability

The data and samples analyzed in the current study are either included in the article and in the supplementary information or can be obtained from the corresponding author on request.

Received: 3 June 2024; Accepted: 4 September 2024
Published online: 17 September 2024

References

1. Fahrenholtz, W. G., Hilmas, G. E., Talmy, I. G. & Zaykoski, J. A. Refractory diborides of zirconium and hafnium. *J. Am. Ceram. Soc.* **90**, 1347–1364 (2007).
2. Zhang, X., Luo, X., Han, J., Li, J. & Han, W. Electronic structure, elasticity and hardness of diborides of zirconium and hafnium: First principles calculations. *Comput. Mater. Sci.* **44**, 411–421 (2008).
3. Mayrhofer, P. H., Mitterer, C., Wen, J. G., Greene, J. E. & Petrov, I. Self-organized nanocolumnar structure in superhard TiB_2 thin films. *Appl. Phys. Lett.* **86**, 131909 (2005).
4. Munro, R. G. Material properties of titanium diboride. *J. Res. Natl. inst. Stand. Technol.* **105**, 709 (2000).
5. Naraparaju, R., Maniya, K., Murchie, A., Fahrenholtz, W. G. & Hilmas, G. E. Effect of moisture on the oxidation behavior of ZrB2. *J. Am. Ceram. Soc.* **104**, 1058–1066 (2021).
6. Fahrenholtz, W. G. & Hilmas, G. E. Oxidation of ultra-high temperature transition metal diboride ceramics. *Int. Mater. Rev.* **57**, 61–72 (2012).
7. Agulov, A. V., Goncharov, A. A., Stupak, V. A. & Petukhov, V. V. Thermal stability of the phase composition and structure of hafnium diboride films. *Inorg Mater* **50**, 460–463 (2014).
8. Bakhit, B. *et al.* Multifunctional ZrB_2-rich $Zr_{1-x}Cr_xB_y$ thin films with enhanced mechanical, oxidation, and corrosion properties. *Vacuum* **185**, 109990 (2021).
9. Monteverde, F. & Scatteia, L. Resistance to thermal shock and to oxidation of metal diborides? SiC ceramics for aerospace application. *J. Am. Ceram. Soc.* **90**, 1130–1138 (2007).
10. Gild, J. *et al.* High-entropy metal diborides: A new class of high-entropy materials and a new type of ultrahigh temperature ceramics. *Sci. Rep.* **6**, 1–10 (2016).
11. Castaing, J. & Costa, P. *In Boron and Refractory Borides* 390–412 (Springer, New York, 1977).
12. Pavese, M., Fino, P., Badini, C., Ortona, A. & Marino, G. HfB_2/SiC as a protective coating for 2D Cf/SiC composites: Effect of high temperature oxidation on mechanical properties. *Surf. Coat. Technol.* **202**, 2059–2067 (2008).
13. Pellegrini, C., Balat-Pichelin, M., Rapaud, O. & Bêche, E. Oxidation resistance of Zr- and Hf-diboride composites containing SiC in air plasma up to 2600 K for aerospace applications. *Ceram. Int.* **48**, 2177–2190 (2022).
14. Dahlqvist, M., Jansson, U. & Rosen, J. Influence of boron vacancies on phase stability, bonding and structure of MB_2 (M = Ti, Zr, Hf, V, Nb, Ta, Cr, Mo, W) with AlB_2 type structure. *J. Phys. Condens. Matter Inst. Phys. J.* **27**, 435702 (2015).
15. Wong-Ng, W., McMurdie, H., Paretzkin, B., Hubbard, C., Dragoo. Powder diffraction file. 038–1398 (1986).
16. Magnuson, M., Hultman, L. & Högberg, H. Review of transition-metal diboride thin films. *Vacuum* **196**, 110567 (2022).
17. Vajeeston, P., Ravindran, P., Ravi, C. & Asokamani, R. Electronic structure, bonding, and ground-state properties of AlB_2-type transition-metal diborides. *Phys. Rev. B* **63**, 045115 (2001).
18. Chatterjee, A., Kumar, N., Abelson, J. R., Bellon, P. & Polycarpou, A. A. Nanoscratch and nanofriction behavior of hafnium diboride thin films. *Wear* **265**, 921–929 (2008).
19. Chatterjee, A., Kumar, N., Abelson, J. R., Bellon, P. & Polycarpou, A. A. Nanowear of hafnium diboride thin films. *Tribol. Trans.* **53**, 731–738 (2010).
20. Jayaraman, S. *et al.* HfB_2 and Hf–B–N hard coatings by chemical vapor deposition. *Surf. Coat. Technol.* **200**, 6629–6633 (2006).
21. Reich, S., Suhr, H., Hankó, K. & Szepes, L. Deposition of thin films of zirconium and hafnium boride by plasma enhanced chemical vapor deposition. *Adv. Mater.* **4**, 650–653 (1992).
22. Chowdhury, S., Polychronopoulou, K., Cloud, A., Abelson, J. R. & Polycarpou, A. A. Nanomechanical and nanotribological behaviors of hafnium boride thin films. *Thin Solid Films* **595**, 84–91 (2015).
23. Bakhit, B. *et al.* Systematic compositional analysis of sputter-deposited boron-containing thin films. *J. Vac. Sci. Technol. A* **39**, 063408 (2021).
24. Glechner, T. *et al.* Influence of the non-metal species on the oxidation kinetics of Hf, HfN, HfC, and HfB_2 coatings. *Mater. Des.* **211**, 110136 (2021).
25. Monteverde, F. & Bellosi, A. The resistance to oxidation of an HfB_2–SiC composite. *J. Eur. Ceram. Soc.* **25**, 1025–1031 (2005).
26. Mallik, M., Ray, K. K. & Mitra, R. Oxidation behavior of hot pressed ZrB_2–SiC and HfB_2–SiC composites. *J. Eur. Ceram. Soc.* **31**, 199–215 (2011).
27. Opeka, M. M., Talmy, I. G., Wuchina, E. J., Zaykoski, J. A. & Causey, S. J. Mechanical, thermal, and oxidation properties of refractory hafnium and zirconium compounds. *J. Eur. Ceram. Soc.* **19**, 2405–2414 (1999).
28. Glechner, T. *et al.* High temperature oxidation resistance of physical vapor deposited Hf-Si-$B_{2\pm z}$ thin films. *Corros. Sci.* **205**, 110413 (2022).
29. Glechner, T. *et al.* Influence of Si on the oxidation behavior of TM-Si-$B_{2\pm z}$ coatings (TM = Ti, Cr, Hf, Ta, W). *Surf. Coat. Technol.* **434**, 128178 (2022).
30. Bakhit, B. *et al.* Improving the high-temperature oxidation resistance of TiB_2 thin films by alloying with Al. *Acta Mater.* **196**, 677–689 (2020).
31. Thörnberg, J. *et al.* Improved oxidation properties from a reduced B content in sputter-deposited TiBx thin films. *Surf. Coat. Technol.* **420**, 127353 (2021).
32. Stüber, M. *et al.* Microstructure of Al-containing magnetron sputtered TiB_2 thin films. *Thin Solid Films* **688**, 137361 (2019).
33. Navidi Kashani, A. H. *et al.* Synthesis and oxidation behavior of $Ti_{0.35}Al_{0.65}By$ (y = 1.7–2.4) coatings. *Surf. Coat. Technol.* **442**, 128190 (2022).
34. Navidi Kashani, A. H. *et al.* Morphology, mechanical properties, and oxidation behavior of stoichiometric $Ti_{0.33-x}AlxB_{0.67}$ coatings (x = 0.04, 0.15, 0.21, and 0.28). *Acta Mater.* **270**, 119829 (2024).
35. Dub, S. N. *et al.* Mechanical properties of $HfB_{2.7}$ nanocrystalline thin films. *J. Superhard Mater.* **33**, 151–158 (2011).
36. Jonsson, L. B., Hedlund, C., Katardjiev, I. V. & Berg, S. Compositional variations of sputter deposited Ti/W barrier layers on substrates with pronounced surface topography. *Thin Solid Films* **348**, 227–232 (1999).

37. Ramarotafika, H. & Lemperiere, G. Influence of a d. c. substrate bias on the resistivity, composition, crystallite size and microstrain of WTi and WTi-N films. *Thin Solid Films* **266**, 267–273 (1995).
38. Bergstrom, D. B., Tian, F., Petrov, I., Moser, J. & Greene, J. E. Origin of compositional variations in sputter-deposited Ti_xW_{1-x} diffusion barrier layers. *Appl. Phys. Lett.* **67**, 3102–3104 (1995).
39. Yamazaki, T., Ikeda, N., Tawara, H. & Sato, M. Investigation of composition uniformity of MoSix sputtering films based on measurement of angular distribution of sputtered atoms. *Thin Solid Films* **235**, 71–75 (1993).
40. Neidhardt, J. *et al.* Experiment and simulation of the compositional evolution of Ti–B thin films deposited by sputtering of a compound target. *J. Appl. Phys.* **104**, 63304 (2008).
41. Mráz, S., Emmerlich, J., Weyand, F. & Schneider, J. M. Angle-resolved evolution of the composition of Cr–Al–C thin films deposited by sputtering of a compound target. *J. Phys. D Appl. Phys.* **46**, 135501 (2013).
42. Lide, D. R. *CRC Handbook of Chemistry and Physics* (CRC Press, Boca Raton, 2004).
43. Vegard, L. Die Konstitution der Mischkristalle und die Raumfllung der Atome. *Z. Physik* **5**, 17–26 (1921).
44. Paier, J. *et al.* Screened hybrid density functionals applied to solids. *J. Chem. Phys.* **124**, 154709 (2006).
45. Birajdar, B., Peranio, N. & Eibl, O. Quantitative boron-analysis using EDX in SEM and TEM. *Microsc. Microanal.* **13**, 290–291 (2007).
46. Parthasarathy, T. A., Rapp, R. A., Opeka, M. & Kerans, R. J. A model for the oxidation of ZrB_2, HfB_2 and TiB_2. *Acta Mater.* **55**, 5999–6010 (2007).
47. Dorri, S. *et al.* Oxidation kinetics of overstoichiometric TiB_2 thin films grown by DC magnetron sputtering. *Corros. Sci.* **206**, 110493 (2022).
48. Cai, X. *et al.* Unmasking the anomalous rapid oxidation of refractory TiB_2 at low temperatures. *J. Eur. Ceram. Soc.* **41**, 5100–5108 (2021).
49. Goldstein, J. I. *et al. Scanning Electron Microscopy and X-ray Microanalysis* (Springer, New York, 2017).
50. Tallman, D. J., Anasori, B. & Barsoum, M. W. A critical review of the oxidation of Ti_2AlC, Ti_3AlC_2 and Cr_2AlC in air. *Mater. Res. Lett.* **1**, 115–125 (2013).
51. Ström, P., Petersson, P., Rubel, M. & Possnert, G. A combined segmented anode gas ionization chamber and time-of-flight detector for heavy ion elastic recoil detection analysis. *Rev. Sci. Instrum.* **87**, 103303 (2016).
52. Zhang, Y. *et al.* Detection efficiency of time-of-flight energy elastic recoil detection analysis systems. *Nucl. Instrum. Methods Phys. Res. Sect. B Beam Interact. Mater. Atoms* **149**, 477–489 (1999).
53. to Baben, M. *et al.* Unprecedented thermal stability of inherently metastable titanium aluminum nitride by point defect engineering. *Mater. Res. Lett.* **5**, 158–169 (2017).
54. Pitthan, E., Moro, M. V., Corrêa, S. A. & Primetzhofer, D. Assessing boron quantification and depth profiling of different boride materials using ion beams. *Surf. Coat. Technol.* **417**, 127188 (2021).
55. Wang, Y. & Nastasi, M. *Handbook of Modern Ion Beam Materials Analysis* (MRS, Materials Research Soc, 2010).
56. Oliver, W. C. & Pharr, G. M. An improved technique for determining hardness and elastic modulus using load and displacement sensing indentation experiments. *J. Mater. Res.* **7**, 1564–1583 (1992).
57. Shein, I. R. & Ivanovskii, A. L. Elastic properties of mono-and polycrystalline hexagonal AlB_2-like diborides of s, p and d metals from first-principles calculations. *J. Phys. Condens. Matter* **20**, 415218 (2008).
58. Zhang, J.-D., Cheng, X.-L. & Li, D.-H. First-principles study of the elastic and thermodynamic properties of HfB_2 with AlB_2 structure under high pressure. *J. Alloys Compd.* **509**, 9577–9582 (2011).
59. Pan, Y., Huang, H., Wang, X. & Lin, Y. Phase stability and mechanical properties of hafnium borides: A first-principles study. *Comput. Mater. Sci.* **109**, 1–6 (2015).
60. Liang, H. *et al.* Study of the compression behavior and elastic properties of HfB_2 ceramics using experimental method and first-principles calculations. *J. Alloys Compd.* **808**, 151764 (2019).
61. Hohenberg, P. & Kohn, W. Inhomogeneous electron gas. *Phys. Rev.* **136**, B864 (1964).
62. Kohn, W. & Sham, L. J. Self-consistent equations including exchange and correlation effects. *Phys. Rev.* **140**, A1133 (1965).
63. Kresse, G. & Furthmüller, J. Efficient iterative schemes for ab initio total-energy calculations using a plane-wave basis set. *Phys. Rev. B* **54**, 11169 (1996).
64. Kresse, G. & Furthmüller, J. Efficiency of ab-initio total energy calculations for metals and semiconductors using a plane-wave basis set. *Comput. Mater. Sci.* **6**, 15–50 (1996).
65. Blöchl, P. E. Projector augmented-wave method. *Phys. Rev. B* **50**, 17953 (1994).
66. Kresse, G. & Joubert, D. From ultrasoft pseudopotentials to the projector augmented-wave method. *Phys. Rev. B* **59**, 1758 (1999).
67. Perdew, J. P., Burke, K. & Ernzerhof, M. Generalized gradient approximation made simple. *Phys. Rev. Lett.* **77**, 3865 (1996).
68. Gehringer, D., Friák, M. & Holec, D. Models of configurationally-complex alloys made simple. *Comput. Phys. Commun.* **286**, 108664 (2023).
69. Momma, K. & Izumi, F. VESTA 3 for three-dimensional visualization of crystal, volumetric and morphology data. *J. Appl. Crystallogr.* **44**, 1272–1276 (2011).
70. Hill, R. The elastic behaviour of a crystalline aggregate. *Proc. Phys. Soc. A* **65**, 349–354 (1952).
71. Yu, R., Zhu, J. & Ye, H. Q. Calculations of single-crystal elastic constants made simple. *Comput. Phys. Commun.* **181**, 671–675 (2010).

Acknowledgements

This research was funded by German Research Foundation (DFG SCHN735/42-1 and DFG SCHN735/47-1). Transnational ion beam analysis access has been supported by the RADIATE project under the Grant Agreement 824096 from the EU Research and Innovation program HORIZON 2020. Accelerator operation at Uppsala University has been supported by the Swedish research council VR-RFI (#2019-00191).

Author contributions

P.K. and J.M.S. conceived the research. P.K. carried out the experiments and L.L and G.K.N. performed the theoretical calculations. S.L., A.H.N.K., M.H., P.J.P, D.M.H., P.S., and D.P. contributed to the sample characterization and data analysis. P.K. and J.M.S. wrote the original draft of this paper. All authors reviewed and edited the manuscript.

Funding

Open Access funding enabled and organized by Projekt DEAL.

Competing interests

The authors declare no competing interests.

Additional information

Supplementary Information The online version contains supplementary material available at https://doi.org/10.1038/s41598-024-72134-3.

Correspondence and requests for materials should be addressed to P.K.

Reprints and permissions information is available at www.nature.com/reprints.

Publisher's note Springer Nature remains neutral with regard to jurisdictional claims in published maps and institutional affiliations.

Open Access This article is licensed under a Creative Commons Attribution 4.0 International License, which permits use, sharing, adaptation, distribution and reproduction in any medium or format, as long as you give appropriate credit to the original author(s) and the source, provide a link to the Creative Commons licence, and indicate if changes were made. The images or other third party material in this article are included in the article's Creative Commons licence, unless indicated otherwise in a credit line to the material. If material is not included in the article's Creative Commons licence and your intended use is not permitted by statutory regulation or exceeds the permitted use, you will need to obtain permission directly from the copyright holder. To view a copy of this licence, visit http://creativecommons.org/licenses/by/4.0/.

© The Author(s) 2024